

Off-Road Navigation via Implicit Neural Representation of Terrain Traversability

Yixuan Jia¹, Qingyuan Li¹, Jonathan P. How¹

Abstract— Autonomous off-road navigation requires robots to estimate terrain traversability from onboard sensors and plan accordingly. Conventional approaches typically rely on sampling-based planners such as MPPI to generate short-term control actions that aim to minimize traversal time and risk measures derived from the traversability estimates. These planners can react quickly but optimize only over a short look-ahead window, limiting their ability to reason about the full path geometry, which is important for navigating in challenging off-road environments. Moreover, they lack the ability to adjust speed based on the terrain bumpiness, which is important for smooth navigation on challenging terrains. In this paper, we introduce TRAIL (Traversability with an Implicit Learned Representation), an off-road navigation framework that leverages an implicit neural representation to continuously parameterize terrain properties. This representation yields spatial gradients that enable integration with a novel gradient-based trajectory optimization method that adapts the path geometry and speed profile based on terrain traversability.

I. INTRODUCTION

Autonomous navigation in off-road environments requires capabilities beyond obstacle avoidance. Unlike urban roads, off-road terrain exhibits highly variable and unstructured conditions such as uneven surfaces and vegetation. Consequently, there has been growing interest in developing autonomous systems capable of operating reliably in these settings [1]–[15].

Most existing off-road navigation frameworks estimate terrain traversability from either terrain geometry [1]–[7] or vehicle traction on the terrain [9]–[15], from which a cost map is derived and represented as a grid map. Methods that rely purely on geometric information can be too conservative as they may struggle to distinguish between drivable vegetation, such as tall grass, and rigid obstacles, such as rocks, since both may appear as regions with high elevation and steep slopes. On the other hand, methods that only rely on traction estimate suffer from generalizability, since the supervision signal can only be generated along the vehicle’s traversed path. Moreover, data must be collected in non-traversable (i.e., possibly dangerous) regions – for example, a robot must actually collide with trees enough times to learn that trees are obstacles. On the planning side, gradient-free sampling-based trajectory optimization techniques such as MPPI [16] are applied to generate a path using the cost grid map. While MPPI offers great flexibility in defining

This work was supported in part by Army’s Research Lab (ARL) under Grant W911NF-21-2-0150 and ARL DCIST under Cooperative Agreement Number W911NF-17-2-0181. Distribution Statement A: Approved for public release; distribution is unlimited.

¹Massachusetts Institute of Technology, Cambridge, MA 02139, USA. {yixuany, andyli27, jhow}@mit.edu.

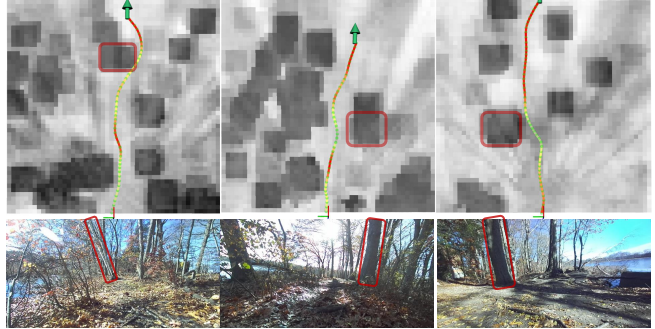


Fig. 1: **Top:** Optimized trajectories overlaid on the blended cost map, generated by combining two cost maps with 50% transparency (sampled at fixed grid resolution for visualization). The larger dark blocks represent higher geometric risk inflated using vehicle radius (e.g. the highlighted tree trunks) while finer greyscale variations correspond to predicted terrain bumpiness (e.g. grey regions around trees from tree roots). Redder trajectory segments indicate higher speed. **Bottom:** Corresponding onboard camera images. The optimized trajectories avoid hard obstacles, slow down when approaching bumpy regions, and speed up in smoother areas.

the objective function, it often produces non-smooth, oscillatory control signals [17], struggles with handling hard constraints [18], and can require extensive tuning of sampling parameters and weights [19]. Moreover, these formulations do not reason about the full path geometry or speed profile along the trajectory, which are crucial for smooth navigation in challenging off-road environments. Failing to consider these longer-term factors can lead to unnecessary hardware stress and increased odometry drift, both of which negatively impact downstream planning and control.

In this work, we address limitations in both perception and planning to achieve more reliable off-road navigation. We estimate both geometric properties and terrain-response signals, and incorporate these complementary sources of information into planning and trajectory optimization. Geometric properties of the terrain provide a conservative yet physically grounded prior, while the terrain-response signals capture how the vehicle actually interacts with the terrain. Our method leverages implicit neural representations [20] to unify perception and planning within a gradient-based trajectory optimization framework, enabling the planner to jointly adapt the path geometry and speed profile to challenging terrain while respecting constraints. In summary, the contributions of our work are:

- A learning-based implicit neural representation that continuously parametrizes both terrain geometric properties and terrain-response signals. This implicit representation provides smooth spatial structure and readily accessible gradients through a lightweight decoder.
- A novel gradient-based trajectory optimization frame-

work that directly exploits gradient information from the implicit representation to jointly adapt the path geometry and speed profile according to terrain traversability, while naturally handling constraints.

- Comprehensive investigations in both simulation and challenging real-world off-road navigation scenarios, demonstrating the effectiveness of the proposed approach compared to conventional frameworks.

II. PROPOSED METHOD

Given an RGB image and a LiDAR point cloud from onboard sensors, the task is to infer continuous terrain attributes over a local region $[x_{\min}, x_{\max}] \times [y_{\min}, y_{\max}]$ in the vehicle frame and use them to navigate to goals provided by some higher-level planner (which we assume to be given).

A. Learning Implicit Representations

We train a DNN that maps the image and point cloud to traversability-relevant terrain properties. The network consists of a shared encoder that fuses the inputs into a bird’s-eye-view (BEV) feature plane, followed by multiple decoders. Each decoder takes a query point and its corresponding BEV feature and outputs a continuous-valued terrain property (e.g., maximum ground elevation). Unlike prior work (e.g. [5], [11], [15]), which predicts fixed-resolution grid maps, our implicit formulation yields lightweight decoders, faster inference (Fig. 4), and direct access to spatial gradients for trajectory optimization.

1) *Encoder*: Our encoder combines Lift-Splat-Shoot (LSS) [21] and PointPillars [22]. Given an image $X \in \mathbb{R}^{C \times H \times W}$, we define d as the desired down-sampling factor. We extract visual features using DI-NOv2 [23], obtaining $X_{\text{dino}} \in \mathbb{R}^{C_{\text{dino}} \times H_p \times W_p}$. These features are compressed with a lightweight 2D convolution block (Conv + GroupNorm + ReLU) to produce $X_{\text{dc}} \in \mathbb{R}^{C_{\text{dc}} \times H_p \times W_p}$. From X_{dc} , we predict depth logits $X_{\text{depth}} \in \mathbb{R}^{D \times H_d \times W_d}$, where $H_d = H/d$ and $W_d = W/d$. We also interpolate X_{dc} to obtain 2D image features $X_{\text{feat}} \in \mathbb{R}^{C_{\text{dc}} \times H_d \times W_d}$. The pair $(X_{\text{feat}}, X_{\text{depth}})$ is lifted to a 3D volumetric feature of size $C_{\text{dc}} \times D \times H_d \times W_d$ via depth unprojection, which is then splatted onto the BEV plane, following LSS. The resulting image BEV features are compressed to $X_{\text{img}} \in \mathbb{R}^{C_{\text{img}} \times Y \times X}$. For LiDAR, we apply PointPillars to obtain point cloud BEV features $X_{\text{pcd}} \in \mathbb{R}^{C_{\text{pcd}} \times Y \times X}$. The image and point cloud BEV features are concatenated and passed through a 2D convolution block to produce C_{bev} channels, followed by a CBAM attention module [24]. The final encoder output is a fused BEV feature map $X_{\text{bev}} \in \mathbb{R}^{C_{\text{bev}} \times Y \times X}$.

2) *Decoder*: Denote the input to the encoder as \mathbf{X} (i.e. an image and a point cloud). Given a query point $p = (p_x, p_y)$, we can obtain the BEV feature $\psi(p, \mathbf{X}) \in \mathbb{R}^{C_{\text{bev}}}$ at p from X_{bev} . Note that $\psi(p, \mathbf{X})$ is differentiable with respect to p , and that $\psi(p, \mathbf{X})$ contains information about neighboring locations as a result of spatial context aggregation by the 2D convolution blocks and CBAM. Then, inspired by [20], we condition the decoder network on both the query point p and the feature $\psi(p, \mathbf{X})$, thus obtaining

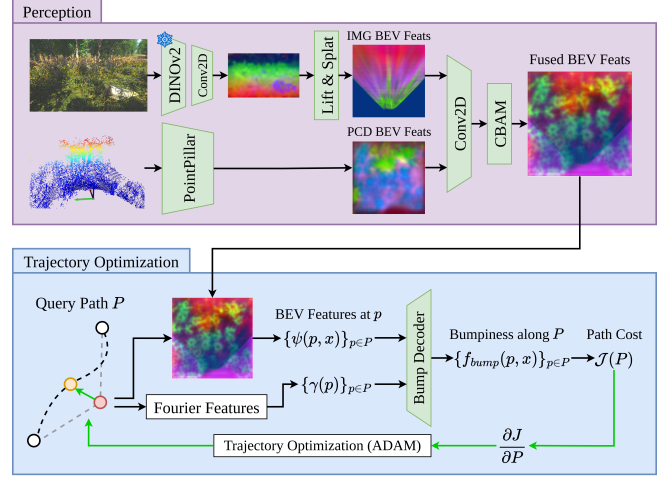


Fig. 2: Our perception module takes a camera image and a LiDAR point cloud and produces an implicit representation of various terrain properties (only the bump decoder is shown). The proposed planning and control framework then incorporates gradient information provided by the implicit representation into a novel gradient-based trajectory optimization framework, where speed profile and path geometry are co-optimized.

an *implicit* representation (also referred to as a coordinate-based representation). However, decoders that take p directly as input can fail to predict high-frequency features [25] such as small rocks or partially buried tree roots, which are important for traversability estimation tasks. Instead, we first obtain Fourier features [25] from p , denoted $\gamma(p) \in \mathbb{R}^{\text{ff_dim}}$, and then pass $\gamma(p)$ to the decoder, where ff_dim denotes the dimension of the Fourier feature. This approach has been shown to improve the performance of coordinate-based MLPs on capturing high-frequency features [25]. To simplify notation, we integrate the BEV feature sampling, Fourier feature mapping, and MLP decoder into a single decoder function $f_{\theta} : \mathbb{R}^2 \rightarrow \mathbb{R}$, defined over the query point p . In this formulation, the query point is first used to extract the corresponding BEV and Fourier features, which are then jointly processed by the MLP decoder, i.e. $p \mapsto (\gamma(p), \psi(p, \mathbf{X})) \mapsto \text{MLP}(\gamma(p), \psi(p, \mathbf{X}))$. Our architecture includes five decoders: $f_{g,\min}, f_{g,\max}, f_{c,\text{mask}}, f_{c,\min}, f_{\text{bump}}$. Two of them estimate the minimum and maximum ground elevations, while two more predict a ceiling mask—indicating the presence of overhanging structures—and the minimum ceiling height, inspired by [26]. The ceiling-related decoders are used exclusively during training to prevent ceilings from being misidentified as ground, thereby avoiding inflated ground elevation estimates. The fifth decoder predicts terrain bumpiness, as defined in Section II-A.3.

3) *Data Preparation and Training*: The ground truth labels for ground elevations and ceiling predictions are generated in similar fashion to TerrainNet [26], where LiDAR scans in the time range $[t - \delta t, t + \delta t]$ are aggregated using odometry to generate dense annotations at time t . Here we use $\delta t = 15$ s. To quantify terrain bumpiness, we use the root-mean-square (RMS) of the vehicle’s vertical acceleration. A qualitative comparison between this measure (with a window length of 0.1s) and traction (defined as the ratio between estimated and commanded velocity [14]) is shown in Figure 3. Note that the RMS of vertical acceleration on the

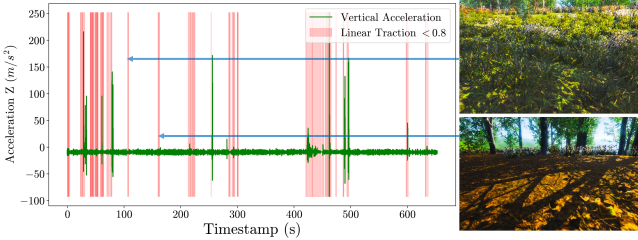


Fig. 3: Comparison of vertical acceleration from an IMU and low-traction events. Peaks in vertical acceleration generally coincide with periods of reduced traction. However, occasional false positives occur due to noisy velocity estimates, leading to misclassified high-traction regions (see right). Camera images are tone- and color-corrected for visibility.

same terrain increases approximately proportionally to the vehicle speed [27]. During dataset generation, we normalize the measured RMS of vertical acceleration by the vehicle speed to compensate for this effect, which is then rescaled to $(0, 1)$ using sigmoid. We call the resulting value *bumpiness*. In our trajectory optimization framework (see Section II-B.2), this proportional relationship is intentionally exploited to encourage the optimizer to adapt the speed profile based on predicted terrain bumpiness. To balance the bumpiness data distribution, we compute a histogram of the bumpiness values and give each bumpiness label a weight that is inversely proportional to its frequency. Finally, for training, instead of using another decoder to predict the terrain slope, we directly leverage the differentiability of $f_{g_{\max}}$. We use PyTorch’s autograd functionality to compute the gradient of $f_{g_{\max}}$ with respect to the query point, $\partial_p f_{g_{\max}}$, and compute the loss by comparing $\partial_p f_{g_{\max}}$ to the ground truth terrain slope. L_1 loss is used for $f_{g_{\min}}, f_{g_{\max}}, f_{c_{\min}}, f_{bump}$ and $\partial_p f_{g_{\max}}$. Cross entropy loss is used for both ceiling mask and depth logits prediction.

B. Planning with Implicit Representations

Our planning stack couples a path planner with a trajectory optimizer that exploits spatial gradients from f_{bump} . The path planner first generates a coarse path based on geometric properties of the terrain. This path is then refined by the trajectory optimizer, which leverages terrain bumpiness to adjust both the path geometry and the speed profile, reducing unnecessary detours and promoting smoother, terrain-aware motion. This stands in contrast to recent off-road navigation frameworks [5], [10]–[12], [14], [15], which do not reason about full-path structure and speed adaptation.

1) *Path Planner*: We use A* [28] to generate an initial path. To construct the A* cost map, we first query $f_{g_{\max}}$ at grid locations sampled at a specified coarse resolution. This efficiently produces a coarse geometric grid, from which we compute two metrics: slope (the spatial gradient of $f_{g_{\max}}$) and step size (the elevation difference between adjacent cells). These metrics are normalized to $[0, 1]$ using the maximum acceptable slope and step size respectively. We take the product of the two metrics to fuse them into a single cost map. In our A* implementation, the traversal cost of an edge between neighboring cells is given by the average cell cost multiplied by the Euclidean distance between cell centers. The heuristic is chosen as the straight-line distance

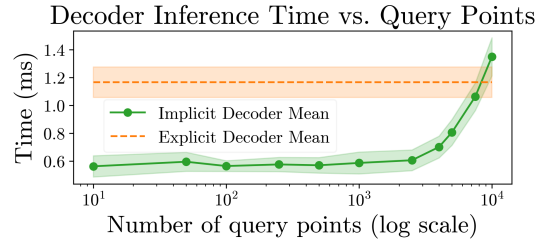


Fig. 4: Inference time for the explicit decoder and implicit decoder vs. number of query points. Note that the explicit decoder outputs a fixed-size 100×100 grid map. Therefore, 10^4 query points to the implicit decoder is equivalent to reconstructing a grid map with the same grid resolution as the explicit decoder. However, for planning and trajectory optimization, the required number of queries is usually far smaller than the full grid size.

to the goal multiplied by the minimum cell cost in the map. Because any feasible path must be at least as long as the Euclidean distance and cannot have a per-meter cost lower than this minimum, the heuristic never overestimates the true cost-to-go and is therefore admissible, while still providing a strong guidance signal for the search.

2) *Trajectory Optimization*: Given an initial path $\{p_i^{\text{init}} = (p_{i,x}^{\text{init}}, p_{i,y}^{\text{init}})\}_{i=1}^{N_p}$ in the local map frame, obtained from A*, we refine it via gradient-based trajectory optimization to minimize travel time and vertical acceleration while ensuring smoothness and dynamic feasibility. We parameterize the geometric path by a set of Catmull–Rom [29] control points $\mathcal{C} = \{c_m\}_{m=1}^M$ with fixed endpoints $c_1 = p_1^{\text{init}}$, $c_M = p_{N_p}^{\text{init}}$ and trainable midpoints $\{c_2, \dots, c_{M-1}\}$. Centripetal Catmull–Rom interpolation [30] yields a dense path $\mathbf{P} = \{p_i\}_{i=1}^N$ ($N > N_p$) sampled along arc length.

From \mathbf{P} we compute segment lengths $\Delta s_i = \|p_{i+1} - p_i\|$ and path curvature κ_i . We evaluate the bumpiness at each path sample p_i by aggregating predictions over a square footprint with side length h , centered at p_i and aligned with the local yaw. This is to account for the vehicle size. Note that each bumpiness prediction is rescaled to be within $(0, 1)$ using sigmoid. The bumpiness prediction b_i at location p_i is then computed by taking the average bumpiness value over the footprint. For each segment i , we then obtain $\bar{b}_i = \frac{1}{2}(b_i + b_{i+1})$ for $i = 1, \dots, N-1$.

We also define a curvature-limited speed cap for each segment i as the smooth minimum [31] of two speed caps:

$$v_{\text{cap},i} = \text{smin}_\tau(v_{\max}, \sqrt{\frac{a_{\text{lat}}^{\max}}{|\kappa_i| + \varepsilon}}) = -\tau \log(e^{-v_{\max}/\tau} + e^{-\left(\sqrt{\frac{a_{\text{lat}}^{\max}}{|\kappa_i| + \varepsilon}}\right)/\tau}),$$

where v_{\max} and a_{lat}^{\max} denote the vehicle’s maximum speed and maximum lateral acceleration. We use the smooth minimum operator, smin , to ensure differentiability. As $\tau \rightarrow 0$, smin_τ converges to \min .

In parallel, a bumpiness-aware preferred speed for each segment i is obtained from a time–bumpiness trade-off:

$$v_{\text{pref},i} = \arg \min_{v>0} \frac{w_{\text{time}}}{v} + w_{\text{bump}} b_i^\alpha v,$$

where $w_{\text{time}}, w_{\text{bump}}$ are weights used to balance trade-offs between travel time and predicted vertical acceleration. The

first term in the objective encourages shorter travel time, while the second term penalizes high vertical acceleration, taking into account that vertical acceleration scales proportionally to vehicle speed multiplied by the bumpiness estimate. The exponent $\alpha \in \mathbb{N}$ in b_i^α helps rescales the bumpiness prediction. Empirically, setting α to a higher value (e.g. 2 or 3 vs. 1) creates a larger contrast in the speed profile (i.e. slowing down more in bumpy regions and speeding up more in smooth regions). Note that the objective is convex in v and the minimizer can be obtained by setting its gradient to 0, which yields $v_{\text{pref},i} = \sqrt{\frac{w_{\text{time}}}{w_{\text{bump}}(b_i^\alpha + \varepsilon)}}$. As before, to ensure differentiability, we fuse the speed cap and the preferred speed using the smooth minimum operator $v_i = \text{smin}_\tau(v_{\text{cap},i}, v_{\text{pref},i})$. Let $\bar{v}_i = \frac{1}{2}(v_i + v_{i+1})$ denote the segment speed and $\bar{\kappa}_i = \frac{1}{2}(\kappa_i + \kappa_{i+1})$ denote the segment curvature. Our objective combines a time surrogate, a speed-weighted bump cost, and geometric regularizers:

$$\mathcal{J}(\mathcal{C}) = \underbrace{\sum_{i=1}^{N-1} \frac{\Delta s_i}{\bar{v}_i}}_{\text{time surrogate}} + \lambda_b \underbrace{\sum_{i=1}^{N-1} \bar{b}_i \bar{v}_i \Delta s_i}_{\text{speed-weighted bump cost}} + \lambda_s \underbrace{\sum_{i=1}^{N-1} (\Delta s_i)^2}_{\text{path smoothness}} + \lambda_\kappa \underbrace{\sum_{i=2}^{N-1} \bar{\kappa}_i^2}_{\text{curvature smoothness}}$$

where $\lambda_b, \lambda_s, \lambda_\kappa$ are weights used to balance different terms. Note that the objective $\mathcal{J}(\mathcal{C})$ is differentiable with respect to \mathbf{P} thanks to the differentiability of f_{bump} with respect to the query points as well as the differentiability of $\bar{v}_i, \bar{\kappa}_i, \Delta s_i$ with respect to \mathbf{P} . Since the interpolation from \mathcal{C} to \mathbf{P} is differentiable, the objective is differentiable with respect to \mathcal{C} , thus enabling gradient-based optimization. We optimize only the interior control points using Adam [32] with gradient clipping, and project them onto the local planning bounds $[x_{\min}, x_{\max}] \times [y_{\min}, y_{\max}]$. Start and goal (i.e. c_1, c_M) are held fixed.

After the optimization, we perform a 1-D time-scaling along arc length to obtain a dynamically feasible velocity profile following standard trajectory time-parameterization approaches [33], [34]. We enforce $v \leq v_{\max}$, $v^2 |\kappa| \leq a_{\text{lat}}^{\max}$, and tangential acceleration limits $a \in [-a_{\text{dec}}, a_{\text{acc}}]$, while retaining the same soft trade-off between time and bump cost to shape the speed profile. Finally, we recover yaw from the path tangent and angular rate via $\omega = v \kappa$, yielding the outputs $\{t, \mathbf{P}, \text{yaw}(t), v(t), \omega(t)\}$.

3) *Tracking Controller*: We formulate an MPC problem to track the optimized trajectory. Let $x = [p_x, p_y, \theta]^T, u = [v, \omega]^T$, where p_x, p_y denote the x, y coordinates of the vehicle, θ denotes the yaw angle, and v, ω denote the linear speed and angular rate. The optimization problem is then:

$$\begin{aligned} \min_{x_1, \dots, x_N, u_0, \dots, u_{N-1}} & \sum_{k=0}^{N-1} \left(\|x_k - x_k^{\text{ref}}\|_Q^2 + \|u_k - u_k^{\text{ref}}\|_R^2 \right. \\ & \quad \left. + \|x_N - x_N^{\text{ref}}\|_{Q_N}^2 \right) \\ \text{s.t. } & x_{k+1} = x_k + \Delta t \begin{bmatrix} \cos(\theta_k) v_k \\ \sin(\theta_k) v_k \\ \omega_k \end{bmatrix} \\ & v_{\min} \leq v_k \leq v_{\max} \\ & \omega_{\min} \leq \omega_k \leq \omega_{\max}, \forall k \in \{0, \dots, N-1\}, \end{aligned}$$

which is solved using **do-mpc** [35]–[37].

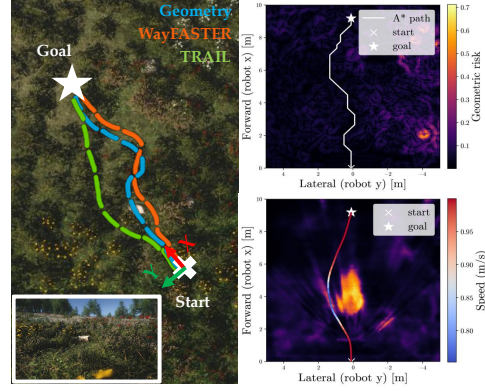


Fig. 5: Grassland scenario. The robot's forward direction (x) and leftward direction (y) are represented by the red and green axes, respectively. Examples of paths produced by Geo-20 (blue), WF-20 (orange), and TRAIL (green) are shown on the left. The bottom left corner shows the camera image from the robot. On the right side, the top shows the initial path generated by A* overlaid on the geometric risk map. Bottom right shows the optimized trajectory overlaid on the predicted bumpiness value. The trajectory is color-coded by speed.

III. SIMULATION EXPERIMENTS

We evaluate the proposed approach on a series of representative off-road navigation scenarios in a Unity simulation environment.

A. Baselines

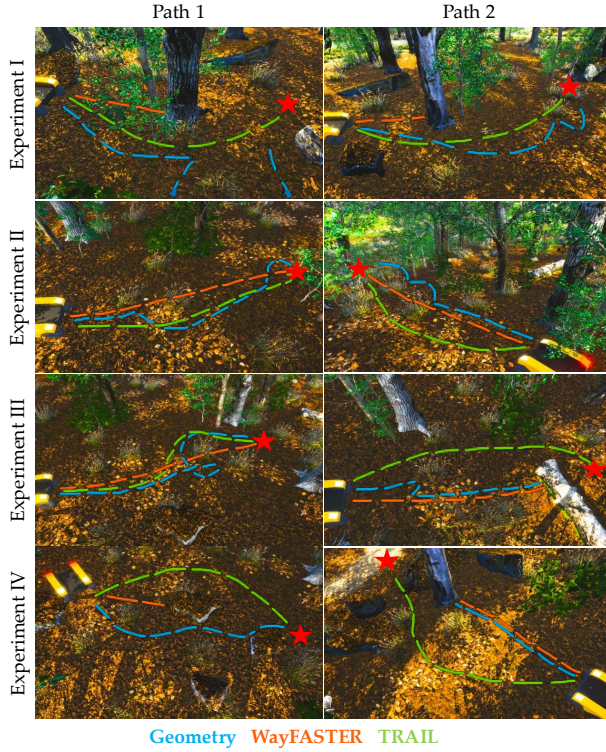
We compare against one geometry-based and one traction-based baseline. For the geometry-based method, we implement a RoadRunner-style method [5]: geometric risk factors (step size, slope, curvature) are fused via Conditional Value at Risk (CVaR) to form a risk map, which is then used by an MPPI controller. Our implementation uses our encoder and the WayFASTER decoder [15] due to lack of publicly available code. We refer to this baseline as **Geometry**. For the traction-based baseline, we use WayFASTER [15] with its released network architecture¹, paired with an MPPI controller following the formulation in the original paper. We implemented both MPPI controllers by adapting a public PyTorch-based codebase². We use a horizon $N = 20$ with a time step of $dt = 0.1s$.

B. Dataset and Training

The training data consists of about 1600s of a robot traversing grassland and forest, where it encounters small rocks and bushes intermittently but avoids trees and large obstacles. As we will see in the results, WayFASTER struggles to learn useful features due to the sparse training signal. The optimizer for both our method and **Geometry** is AdamW [38] with a learning rate of 5×10^{-5} and a weight decay of 10^{-4} . A cosine annealing scheduler [39] is applied with $T_{\max} = 10$ and $\eta_{\min} = 10^{-5}$ to gradually reduce the learning rate during training. The optimizer for WayFASTER is as provided in their codebase. Each method is trained for 100 epochs with a batch size of 4, and the best checkpoint is used.

¹<https://github.com/matval/wayfastr>

²https://github.com/UM-ARM-Lab/pytorch_mppt



Geometry WayFASTER TRAIL

Fig. 6: Forest scenario. Each row shows one set of experiments. The first column shows Path 1 and the second column shows Path 2 of each set of experiments. The forest consists of tall grass, bushes, rocks, logs, and trees. Images are tone- and color-corrected for visibility. The proposed method is able to navigate efficiently while the two baselines struggle: Geometry is conservative due to the density of objects with high elevations while WayFASTER is too optimistic since there are no collision events with similar objects in the training data. On the other hand, our method is able to recognize and avoid rocks while not being constrained by the tall grass.

C. Metric

To evaluate each method, we repeat every run three times and report the following: Success Rate (percentage of runs reaching the goal), Progress (fraction of initial distance covered), Time (time to reach the goal), Length (total path length), Mean and Max Vertical Acceleration RMS (computed over a 0.1s window). Runs that exceed the 60s time cap are marked as failures. All metrics except Success Rate and Progress are computed only on successful runs.

D. Timing Analysis

Timings are performed on a workstation with an RTX 4090 GPU, an AMD Ryzen 9 7950x 16-core processor with 32 threads, and 128 GB of RAM. A detailed analysis of decoder timing is shown in Figure 4. The encoder of our model and Geometry take 25ms per inference and WayFASTER’s encoder takes 20ms. With horizon $N = 20$, Geometry’s MPPI takes 10ms per inference and WayFASTER’s MPPI takes 25ms per inference. For the proposed method, A* takes 5 ms (to generate a path with 40 points), trajectory optimization takes 7.5 ms per iteration (to optimize an initial path with 30 points, which are downsampled from the A* path), and the MPC take 6ms with horizon $N = 20$.

TABLE I: Comparison Results (Grassland)

Metric	Geo-20	Geo-50	Way-20	Way-50	TRAIL
Success [%]	100.0	100.0	66.7	100.0	100.0
Progress [%]	100.0 ± 0.0	100.0 ± 0.0	76.0 ± 33.9	100.0 ± 0.0	100.0 ± 0.0
Time [s]	21.3 ± 1.9	60.5 ± 0.3	<u>16.6 ± 2.3</u>	17.2 ± 2.0	12.0 ± 0.4
Length [m]	<u>10.7 ± 0.5</u>	14.3 ± 1.1	11.7 ± 1.2	11.9 ± 0.9	10.3 ± 0.4
Vert. Acc. RMS [m s^{-2}]	2.8 ± 0.1	2.7 ± 0.1	<u>2.5 ± 0.3</u>	2.6 ± 0.5	1.8 ± 0.3
Vert. Acc. Max [m s^{-2}]	75.8 ± 6.6	72.8 ± 47.5	<u>43.4 ± 23.4</u>	58.7 ± 15.9	4.4 ± 0.5

TABLE II: Comparison Results (Forest)

Method	Success (%)	Progress (%)	Time (s)	Length (m)	Acc (m/s^2)		
					RMS	Max	
Forest Experiment I							
Path 1	Geometry	100.0	100.0 ± 0.0	<u>44.0 ± 1.6</u>	<u>24.0 ± 1.5</u>	<u>1.8 ± 0.1</u>	<u>6.1 ± 0.3</u>
	WayFASTER	0.0	60.8 ± 4.6	N/A	N/A	N/A	N/A
	TRAIL	100.0	100.0 ± 0.0	<u>11.5 ± 2.2</u>	<u>11.4 ± 2.2</u>	<u>1.7 ± 0.1</u>	6.0 ± 1.7
Path 2	Geometry	100.0	100.0 ± 0.0	<u>38.3 ± 14.2</u>	<u>20.9 ± 9.0</u>	<u>1.8 ± 0.1</u>	<u>6.2 ± 0.1</u>
	WayFASTER	0.0	31.3 ± 2.3	N/A	N/A	N/A	N/A
	TRAIL	100.0	100.0 ± 0.0	<u>10.9 ± 1.1</u>	<u>10.8 ± 1.0</u>	<u>1.7 ± 0.1</u>	5.1 ± 0.7
Forest Experiment II							
Path 1	Geometry	100.0	100.0 ± 0.0	<u>26.8 ± 6.7</u>	<u>14.2 ± 1.3</u>	<u>1.9 ± 0.2</u>	5.5 ± 0.5
	WayFASTER	100.0	100.0 ± 0.0	<u>11.5 ± 1.8</u>	<u>10.9 ± 0.9</u>	<u>1.8 ± 0.2</u>	5.5 ± 0.8
	TRAIL	100.0	100.0 ± 0.0	10.9 ± 0.4	10.9 ± 0.4	1.8 ± 0.1	6.0 ± 0.3
Path 2	Geometry	33.3	91.3 ± 6.2	45.3 ± 0.0	22.3 ± 0.0	1.9 ± 0.0	6.2 ± 0.0
	WayFASTER	100.0	100.0 ± 0.0	<u>13.3 ± 1.7</u>	12.1 ± 0.8	<u>1.9 ± 0.1</u>	5.8 ± 0.2
	TRAIL	100.0	100.0 ± 0.0	<u>12.3 ± 0.7</u>	<u>12.5 ± 1.0</u>	<u>1.7 ± 0.1</u>	5.5 ± 0.5
Forest Experiment III							
Path 1	Geometry	100.0	100.0 ± 0.0	<u>52.9 ± 10.4</u>	<u>19.1 ± 3.0</u>	<u>1.7 ± 0.1</u>	<u>14.3 ± 12.7</u>
	WayFASTER	100.0	100.0 ± 0.0	<u>10.8 ± 0.1</u>	10.4 ± 0.1	<u>1.8 ± 0.0</u>	5.7 ± 0.4
	TRAIL	100.0	100.0 ± 0.0	<u>10.9 ± 0.3</u>	<u>11.0 ± 0.2</u>	<u>1.7 ± 0.1</u>	4.5 ± 0.7
Path 2	Geometry	0.0	<u>67.0 ± 1.2</u>	N/A	N/A	N/A	N/A
	WayFASTER	0.0	<u>61.3 ± 1.5</u>	N/A	N/A	N/A	N/A
	TRAIL	66.7	91.5 ± 12.1	<u>12.9 ± 0.5</u>	<u>11.6 ± 0.1</u>	<u>2.0 ± 0.4</u>	31.6 ± 37.0
Forest Experiment IV							
Path 1	Geometry	66.7	79.1 ± 29.5	<u>33.5 ± 11.8</u>	<u>13.7 ± 1.3</u>	<u>4.0 ± 1.7</u>	<u>79.3 ± 54.0</u>
	WayFASTER	0.0	<u>14.0 ± 14.0</u>	N/A	N/A	N/A	N/A
	TRAIL	100.0	100.0 ± 0.0	<u>12.7 ± 0.2</u>	<u>12.5 ± 0.2</u>	<u>1.9 ± 0.2</u>	5.1 ± 0.8
Path 2	Geometry	0.0	<u>60.4 ± 4.2</u>	N/A	N/A	N/A	N/A
	WayFASTER	0.0	<u>57.6 ± 1.5</u>	N/A	N/A	N/A	N/A
	TRAIL	100.0	100.0 ± 0.0	<u>15.3 ± 1.9</u>	<u>14.7 ± 1.3</u>	<u>3.6 ± 0.3</u>	52.2 ± 17.8

E. Navigation Performance

Grassland The Grassland scenario (see Figure 5) features a rock hidden in tall grass (bottom left of Figure 5). The quantitative results in Table I show that Geometry, whose inflated geometric map cannot distinguish the rock from tall grass, produces an almost uniform risk map, drives straight toward the goal, runs over the rock, and incurs large vertical acceleration (Geo-20). Because CVaR values lie in $[0, 1]$ [5], MPPI’s behavior is highly sensitive to the trade-off between risk and goal distance: high risk weight leads to oscillations and failure to reach the goal, while low risk weight reproduces Geometry’s straight-line behavior, consistent with our ablation study in Section III-F. WayFASTER detects the rock but is overly optimistic, briefly clipping it and producing high vertical acceleration (WF-20), likely due to weak BEV cues from sparse supervision and a limited encoder. In contrast, our method maintains clearance, using bumpiness during trajectory optimization to push the path away from the rock while remaining less conservative in grass, yielding a smoother, shorter trajectory and an adaptive speed profile that slows near the rock and accelerates through grass. Increasing the MPPI horizon from 20 to 50 confirms that the baselines are not horizon-limited: Geo-50 becomes indecisive and slower due to accumulated risk, while WF-50 matches WF-20 (the single WF-20 failure resulted from odometry divergence). Thus, we use $N = 20$ for subsequent experiments.

Forest To further investigate the performance of the different

methods, we pick 8 paths in a forest that represent different challenges, grouped into 4 sets of experiments, as shown in Figure 6. The forest has trees, rocks, fallen logs, bushes, and tall grass. However, unlike in the training dataset, most rocks in the forest are covered with leaves, making them visually indistinguishable from the ground. Across the four sets of experiments, the baseline methods exhibit distinct failure modes: in Experiment I, *Geometry* reaches the goal but takes long, oscillatory detours around tall grass, whereas *WayFASTER* fails entirely by classifying the tree as traversable due to lack of similar training samples. In Experiment II, all methods reach the goal, but *Geometry* again oscillates in tall grass, while our method takes a slightly longer path yet achieves higher average speed and lower overall vertical acceleration (recall that vertical acceleration scales proportionally to vehicle speed). In Experiment III, *WayFASTER* incorrectly treats the log as traversable, and *Geometry* incorrectly treats the surrounding grass and bush as untraversable—leaving no viable path—whereas our method succeeds in 2 of 3 trials, with the single failure caused by an odometry divergence after a wheel struck the tree trunk. In Experiment IV, *WayFASTER* fails to detect leaf-covered rocks and drives into the “bug trap”, while *Geometry* becomes overly conservative and also gets stuck. Our method avoids the trap (Path 1), identifies the small clearing around the tree (Path 2), and reaches the goal, with vertical acceleration mainly attributable to unavoidable low rocks.

F. Ablation Study

TABLE III: Ablation Study Results (Grassland)

Metric	TRAIL	MPPI-Geo	MPPI-Geo-Term	MPPI-Bump	MPPI-A*+Bump	MPPI-Fused
Success [%]	100.0	0.0	100.0	100.0	100.0	100.0
Progress [%]	100.0 \pm 0.0	9.1 \pm 3.2	100.0 \pm 0.0	100.0 \pm 0.0	100.0 \pm 0.0	100.0 \pm 0.0
Time [s]	12.0 \pm 0.4	N/A	17.3 \pm 2.2	17.2 \pm 0.4	54.8 \pm 4.6	35.6 \pm 18.4
Length [m]	10.3 \pm 0.4	N/A	11.1 \pm 0.7	10.6 \pm 0.2	15.5 \pm 0.6	14.2 \pm 3.5
Vert. Acc. RMS [m s^{-2}]	1.8 \pm 0.3	N/A	3.0 \pm 0.3	2.0 \pm 0.3	1.9 \pm 0.2	2.8 \pm 0.6
Vert. Acc. Max [m s^{-2}]	4.4 \pm 0.5	N/A	61.4 \pm 26.6	21.5 \pm 23.7	41.6 \pm 26.1	87.3 \pm 9.2

To evaluate the proposed planner, we conduct an ablation study by generating fixed-resolution cost maps from our trained model and using MPPI as the planner, following common practice. We implement five variants:

- MPPI-Geo: uses the same geometric cost map as A^* .
- MPPI-Geo-Term: same as MPPI-Geo, but with a $5 \times$ higher terminal-cost weight.
- MPPI-Bump: uses the predicted bumpiness as the cost.
- MPPI- A^* -Bump: initializes MPPI with an A^* path while minimizing bump cost.
- MPPI-Fused: averages the geometric and bumpiness maps to form a fused cost.

In summary, each MPPI formulation minimizes the distance to goal and cost along the path, with a small penalty on control effort. MPPI- A^* -Bump has an additional cost term that penalizes deviations from the initial path. The planning horizon is set to $N = 20$ with $dt = 0.1\text{s}$ for all variants.



Fig. 7: GPS locations of the robot during the long path navigation experiment. The total length is about 370m.

The result is recorded in Table III. MPPI-Geo is unable to reach the goal due to the high geometric risk. On the other hand, MPPI-Geo-Term is able to reach the goal due to a higher terminal-cost weight. However, it is unable to distinguish between traversable vs. un-traversable areas and ends up going straight towards the goal, experiencing large vertical acceleration. Note that the behavior of MPPI-Geo-Term is similar to Geo-20 (see Table I). MPPI-Bump performs the second best, exhibiting similar behavior to Way-20. However, it has a much lower max vertical acceleration, due to the better prediction from our network. MPPI-Geo-Term takes significantly longer to reach the goal due to its conflicting objectives. Similarly, MPPI-Fused takes more time to reach the goal while experiencing large vertical acceleration.

IV. FIELD EXPERIMENTS

We further compare TRAIL with the two baseline methods in real-world hardware experiments. We used an AgileX Scout Mini equipped with a ZED 2i stereo camera and an Ouster OS1-32-GEN2.0 LiDAR. The training data consists of less than 2000 samples, which were all obtained around an area similar to the testing area but with a Clearpath Husky A300 UGV that has the same sensor stack as the Scout. The training data consists of the Husky driving over dirt, paved road, tall grass, tree roots, and branches on the ground, but with no purposeful collision with trees. During data collection, we observed significant odometry drift in the data collected using the Scout Mini (despite post-processing and parameter tuning) due to noisy sensor readings caused by the challenging terrain, which is not ideal for generating training labels. In contrast, the Husky has smoother sensor readings due to its greater mass and better traction, which helps reduces odometry drift. Note that this introduces a distribution shift during testing. We used KISS ICP [40] to generate the odometry used in training data processing, since we found that it generated better odometry during offline processing with minimal tuning, and DLIO [41] to provide odometry at a higher rate during field deployment.

A. Short Path Navigation

We chose five sets of experiments to test the capability of all methods in scenarios that present different challenges. Each set of experiments consists of three trials per method. A trial is considered failed if the vehicle ends up in an unrecoverable configuration (e.g. in collision with a tree trunk), in which case we manually terminated the trial. We set the planning horizon of both baseline approaches to 5.0s (used in [5] for larger scale experiments) and the number of MPPI samples to 4096. Quantitative results are recorded in Table IV and visualizations are shown in Figure 8. Experiments I and IV are challenging due to tree trunks and roots,



Fig. 8: Short Path Navigation Results. Each column shows one set of experiments with separate trials colored differently. The first row shows the paths followed by Geometry, the second row shows the paths followed by WayFASTER, and the third row shows the paths followed by TRAIL. The visualizations are obtained by projecting the odometry to the onboard camera image captured at the starting position.

TABLE IV: Hardware Short Path Navigation Comparison Results

Method	Success (%)	Progress (%)	Time (s)	Length (m)	Vert Acc	Vert Acc
					RMS (m s ⁻²)	Max (m s ⁻²)
Experiment I						
Geometry	33.3	75.7 ± 17.2	28.7 ± 0.0	12.7 ± 0.0	2.0 ± 0.0	18.4 ± 0.0
WayFASTER	0.0	72.0 ± 10.3	N/A	N/A	N/A	N/A
TRAIL	100.0	100.0 ± 0.0	16.6 ± 1.0	13.6 ± 0.9	2.8 ± 0.2	11.9 ± 1.5
Experiment II						
Geometry	0.0	60.0 ± 9.3	N/A	N/A	N/A	N/A
WayFASTER	33.3	72.2 ± 19.7	19.3 ± 0.0	15.4 ± 0.0	1.9 ± 0.0	7.1 ± 0.0
TRAIL	66.7	85.8 ± 20.1	16.2 ± 0.0	15.3 ± 0.6	1.9 ± 0.1	8.9 ± 0.6
Experiment III						
Geometry	0.0	40.1 ± 3.1	N/A	N/A	N/A	N/A
WayFASTER	0.0	37.4 ± 0.4	N/A	N/A	N/A	N/A
TRAIL	66.7	91.1 ± 12.5	14.7 ± 0.6	11.1 ± 0.9	2.1 ± 0.2	11.9 ± 2.6
Experiment IV						
Geometry	100.0	100.0 ± 0.0	28.2 ± 5.1	13.4 ± 1.4	2.0 ± 0.3	11.0 ± 1.5
WayFASTER	0.0	43.0 ± 19.9	N/A	N/A	N/A	N/A
TRAIL	100.0	100.0 ± 0.0	16.3 ± 1.2	11.5 ± 0.2	2.9 ± 0.3	10.8 ± 1.5
Experiment V						
Geometry	0.0	14.5 ± 14.5	N/A	N/A	N/A	N/A
WayFASTER	0.0	67.6 ± 23.5	N/A	N/A	N/A	N/A
TRAIL	100.0	100.0 ± 0.0	24.2 ± 1.7	18.6 ± 1.1	1.4 ± 0.0	7.1 ± 0.2

Experiment II involves tall vegetation, and Experiments III and V combine both scenarios.

Geometry failed all experiments with tall but traversable vegetation, exhibiting behavior similar to that observed in the simulation study. It succeeded in only one of three trials in Experiment I, primarily due to indecisive behavior, oscillating between left- and right-side avoidance (from MPPI sampling trajectories on both sides of the tree). Geometry was able to navigate successfully in Experiment IV, but it had a longer travel time due to its indecisive behavior near the goal, which was located in a region with high geometric risk.

WayFASTER failed all the experiments with geometric obstacles, which is consistent with the simulation study. It only succeeded in one of three trials in Experiment II (colored with yellow), where the other trials failed due to collision with a non-traversable thin tree.

We observe that TRAIL has an overall higher success rate and is able to navigate efficiently without incurring large experienced vertical acceleration (note again that vertical ac-

celeration scales with vehicle speed and TRAIL has a greater average speed). Moreover, TRAIL generally exhibits more deterministic behavior. The only exception is Experiment III, where two of the three trials took a detour to avoid areas with short tree trunks and tall grass, while the third navigated directly through that region. This deviation is caused by the slight stochasticity of the network’s predictions, caused by sensor noise, which produced a small clearing in the geometric risk map for that particular run. In Experiment V, TRAIL found a clearing (paved road) on the right side and thus takes a detour. From the observed behaviors of all three methods, we attribute TRAIL’s superior overall performance to two key factors: its ability to conduct trajectory optimization that considers the full path rather than relying purely on reactive planning, and its ability to modulate the speed profile using the predicted bumpiness of the terrain.

B. Long Path Navigation

We also conducted a long path navigation experiment with TRAIL; the overall route is illustrated in Figure 7. A total of eight interventions were required: five were caused by the platform’s limited traction on wet ground (training data was collected on a sunny day with dry ground), and three were caused by planned trajectories that would have resulted in collisions. Of these three interventions, two were due to small trees that were outside the camera’s field of view and within LiDAR blind spots created by the sensor-stack pillars. The remaining intervention was caused by the trajectory optimizer overly smoothing a pair of consecutive tight turns that were intended to avoid two nearby trees.

C. Limitations

After conducting more tests in the area, we observed that sensor occlusion and field-of-view limitations are a main failure mode of TRAIL. Potential solutions include temporal fusion of sensor information.

V. CONCLUSION

In this work, we proposed and evaluated an off-road navigation framework. The framework consists of a percep-

tion module that learns an implicit representation of terrain properties and a planner that utilizes the gradient information from the perception module to perform gradient-based trajectory optimization. The proposed approach is able to navigate effectively in challenging environments. Although we mainly focus on off-road navigation tasks in this paper, the trajectory optimization framework that leverages an implicit neural representation can be applied to a broad class of navigation problems. One future direction is temporal fusion of the traversability prediction to enable longer range navigation and to overcome sensor occlusion.

REFERENCES

- [1] D. D. Fan, K. Otsu, Y. Kubo, A. Dixit, J. Burdick, and A.-A. Agha-Mohammadi, “Step: Stochastic traversability evaluation and planning for risk-aware off-road navigation,” *arXiv preprint arXiv:2103.02828*.
- [2] Z. Jian, Z. Lu, X. Zhou, B. Lan, A. Xiao, X. Wang, and B. Liang, “Putn: A plane-fitting based uneven terrain navigation framework,” in *2022 IEEE/RSJ International Conference on Intelligent Robots and Systems*. IEEE, 2022, pp. 7160–7166.
- [3] H. Xue, H. Fu, L. Xiao, Y. Fan, D. Zhao, and B. Dai, “Traversability analysis for autonomous driving in complex environment: A lidar-based terrain modeling approach,” *Journal of Field Robotics*, 2023.
- [4] A. Dixit, D. D. Fan, K. Otsu, S. Dey, A.-A. Agha-Mohammadi, and J. Burdick, “Step: Stochastic traversability evaluation and planning for risk-aware navigation: results from the darpa subterranean challenge,” *Field Robotics*, vol. 4, pp. 182–210, 2024.
- [5] J. Frey, M. Patel, D. Atha, J. Nubert, D. Fan, A. Agha, C. Padgett, P. Spieler, M. Hutter, and S. Khattak, “Roadrunner-learning traversability estimation for autonomous off-road driving,” *IEEE Transactions on Field Robotics*, 2024.
- [6] M. Patel, J. Frey, D. Atha, P. Spieler, M. Hutter, and S. Khattak, “RoadRunner M&M-learning multi-range multi-resolution traversability maps for autonomous off-road navigation,” *IEEE Robotics and Automation Letters*, 2024.
- [7] S.-W. Yoo, E.-I. Son, and S.-W. Seo, “Traversability-aware adaptive optimization for path planning and control in mountainous terrain,” *IEEE Robotics and Automation Letters*, 2024.
- [8] D. Lee, I. M. A. Nahrendra, M. Oh, B. Yu, and H. Myung, “TRG-Planner: Traversal risk graph-based path planning in unstructured environments for safe and efficient navigation,” *IEEE Robotics and Automation Letters*, 2025.
- [9] J. Frey, M. Mattamala, N. Chebrolu, C. Cadena, M. Fallon, and M. Hutter, “Fast traversability estimation for wild visual navigation,” *arXiv preprint arXiv:2305.08510*, 2023.
- [10] X. Cai, M. Everett, L. Sharma, P. R. Osteen, and J. P. How, “Probabilistic traversability model for risk-aware motion planning in off-road environments,” in *2023 IEEE/RSJ International Conference on Intelligent Robots and Systems*. IEEE, 2023, pp. 11 297–11 304.
- [11] X. Cai, S. Ancha, L. Sharma, P. R. Osteen, B. Bucher, S. Phillips, J. Wang, M. Everett, N. Roy, and J. P. How, “Evora: Deep evidential traversability learning for risk-aware off-road autonomy,” *IEEE Transactions on Robotics*, 2024.
- [12] X. Cai, J. Queeney, T. Xu, A. Datar, C. Pan, M. Miller, A. Flather, P. R. Osteen, N. Roy, X. Xiao, *et al.*, “Pietra: Physics-informed evidential learning for traversing out-of-distribution terrain,” *IEEE Robotics and Automation Letters*, 2025.
- [13] M. Mattamala, J. Frey, P. Libera, N. Chebrolu, G. Martius, C. Cadena, M. Hutter, and M. Fallon, “Wild visual navigation: Fast traversability learning via pre-trained models and online self-supervision,” *Autonomous Robots*, vol. 49, no. 3, pp. 1–18, 2025.
- [14] M. V. Gasparino, A. N. Sivakumar, Y. Liu, A. E. Velasquez, V. A. Higuti, J. Rogers, H. Tran, and G. Chowdhary, “Wayfast: Navigation with predictive traversability in the field,” *IEEE Robotics and Automation Letters*, vol. 7, no. 4, pp. 10 651–10 658, 2022.
- [15] M. V. Gasparino, A. N. Sivakumar, and G. Chowdhary, “Wayfaster: a self-supervised traversability prediction for increased navigation awareness,” in *2024 IEEE International Conference on Robotics and Automation (ICRA)*. IEEE, 2024, pp. 8486–8492.
- [16] G. Williams, N. Wagener, B. Goldfain, P. Drews, J. M. Rehg, B. Boots, and E. A. Theodorou, “Information theoretic mpc for model-based reinforcement learning,” in *2017 IEEE international conference on robotics and automation (ICRA)*. IEEE, 2017, pp. 1714–1721.
- [17] E. M. Andrejev, A. Manoharan, K.-E. Unt, and A. K. Singh, “ π -MPPI: A projection-based model predictive path integral scheme for smooth optimal control of fixed-wing aerial vehicles,” *IEEE Robotics and Automation Letters*, 2025.
- [18] L. Park, K. Jang, and S. Kim, “Csc-mppi: A novel constrained mpni framework with dbscan for reliable obstacle avoidance,” *arXiv preprint arXiv:2506.16386*, 2025.
- [19] H. Homburger, F. Messerer, M. Diehl, and J. Reuter, “Optimality and suboptimality of mpni control in stochastic and deterministic settings,” *IEEE Control Systems Letters*, 2025.
- [20] S. Peng, M. Niemeyer, L. Mescheder, M. Pollefeys, and A. Geiger, “Convolutional occupancy networks,” in *European Conference on Computer Vision*. Springer, 2020, pp. 523–540.
- [21] J. Philion and S. Fidler, “Lift, splat, shoot: Encoding images from arbitrary camera rigs by implicitly unprojecting to 3d,” in *European conference on computer vision*. Springer, 2020, pp. 194–210.
- [22] A. H. Lang, S. Vora, H. Caesar, L. Zhou, J. Yang, and O. Beijbom, “Pointpillars: Fast encoders for object detection from point clouds,” in *Proceedings of the IEEE/CVF conference on computer vision and pattern recognition*, 2019, pp. 12 697–12 705.
- [23] M. Oquab, T. Dariseti, T. Moutakanni, H. Vo, M. Szafraniec, V. Khalidov, P. Fernandez, D. Haziza, F. Massa, A. El-Nouby, *et al.*, “Dinov2: Learning robust visual features without supervision,” *arXiv preprint arXiv:2304.07193*, 2023.
- [24] S. Woo, J. Park, J.-Y. Lee, and I. S. Kweon, “Cbam: Convolutional block attention module,” in *Proceedings of the European conference on computer vision (ECCV)*, 2018, pp. 3–19.
- [25] M. Tancik, P. Srinivasan, B. Mildenhall, S. Fridovich-Keil, N. Raghavan, U. Singhral, R. Ramamoorthi, J. Barron, and R. Ng, “Fourier features let networks learn high frequency functions in low dimensional domains,” *Advances in neural information processing systems*, vol. 33, pp. 7537–7547, 2020.
- [26] X. Meng, N. Hatch, A. Lambert, A. Li, N. Wagener, M. Schmittel, J. Lee, W. Yuan, Z. Chen, S. Deng, *et al.*, “Terrainnet: Visual modeling of complex terrain for high-speed, off-road navigation,” *arXiv preprint arXiv:2303.15771*, 2023.
- [27] G. A. Pereira, L. C. Pimenta, A. R. Fonseca, L. d. Q. Corrêa, R. C. Mesquita, L. Chaimowicz, D. S. De Almeida, and M. F. Campos, “Robot navigation in multi-terrain outdoor environments,” *The International Journal of Robotics Research*, 2009.
- [28] P. E. Hart, N. J. Nilsson, and B. Raphael, “A formal basis for the heuristic determination of minimum cost paths,” *IEEE transactions on Systems Science and Cybernetics*, vol. 4, no. 2, pp. 100–107, 1968.
- [29] E. Catmull and R. Rom, “A class of local interpolating splines,” in *Computer aided geometric design*. Elsevier, 1974, pp. 317–326.
- [30] C. Yuksel, S. Schaefer, and J. Keyser, “On the parameterization of catmull-rom curves,” in *2009 SIAM/ACM Joint Conference on Geometric and Physical Modeling*, 2009, pp. 47–53.
- [31] Y. Nesterov, “Smooth minimization of non-smooth functions,” *Mathematical programming*, vol. 103, no. 1, pp. 127–152, 2005.
- [32] D. P. Kingma, “Adam: A method for stochastic optimization,” *arXiv preprint arXiv:1412.6980*, 2014.
- [33] J. E. Bobrow, S. Dubowsky, and J. S. Gibson, “Time-optimal control of robotic manipulators along specified paths,” *The international journal of robotics research*, vol. 4, no. 3, pp. 3–17, 1985.
- [34] H. Pham and Q.-C. Pham, “A new approach to time-optimal path parameterization based on reachability analysis,” *IEEE Transactions on Robotics*, vol. 34, no. 3, pp. 645–659, 2018.
- [35] F. Fiedler, B. Karg, L. Lüken, D. Brandner, M. Heinlein, F. Brabender, and S. Lucia, “do-mpc: Towards fair nonlinear and robust model predictive control,” *Control Engineering Practice*, 2023.
- [36] J. A. Andersson, J. Gillis, G. Horn, J. B. Rawlings, and M. Diehl, “CasADi: a software framework for nonlinear optimization and optimal control,” *Mathematical Programming Computation*, 2019.
- [37] A. Wächter and L. T. Biegler, “On the implementation of an interior-point filter line-search algorithm for large-scale nonlinear programming,” *Mathematical programming*, vol. 106, no. 1, pp. 25–57, 2006.
- [38] I. Loshchilov and F. Hutter, “Decoupled weight decay regularization,” *International Conference on Learning Representations (ICLR)*, 2019.
- [39] ———, “SGDR: Stochastic gradient descent with warm restarts,” *International Conference on Learning Representations (ICLR)*, 2017.

- [40] I. Vizzo, T. Guadagnino, B. Mersch, L. Wiesmann, J. Behley, and C. Stachniss, “Kiss-icp: In defense of point-to-point icp–simple, accurate, and robust registration if done the right way,” *IEEE Robotics and Automation Letters*, vol. 8, no. 2, pp. 1029–1036, 2023.
- [41] K. Chen, R. Nemiroff, and B. T. Lopez, “Direct lidar-inertial odometry: Lightweight lio with continuous-time motion correction,” *arXiv preprint arXiv:2203.03749*, 2022.